Low-temperature thermoelectric, galvanomagnetic, and thermodynamic properties of the type-I clathrate $Ba_8Au_xSi_{46-x}$

U. Aydemir, C. Candolfi,* A. Ormeci, Y. Oztan, M. Baitinger, N. Oeschler, F. Steglich, and Yu. Grin
Max-Planck-Institut für Chemische Physik fester Stoffe, Nöthnitzer Straße 40, 01187 Dresden, Germany
(Received 29 August 2011; revised manuscript received 2 November 2011; published 28 November 2011)

Polycrystalline samples of the clathrate $Ba_8Au_xSi_{46-x}$ were synthesized for $0.2 \leqslant x \leqslant 10$. The homogeneity range of the type-I clathrate phase was determined to be $3.63 \leqslant x \leqslant 6.10$ after annealing at 900 °C, while a lower Au concentration ($x \approx 2.2$) was obtained by steel-quenching. Quasisingle phase materials were obtained for $4.10 \leqslant x \leqslant 6.10$. In this composition range, thermoelectric properties, including electrical resistivity, thermopower, and thermal conductivity, were investigated between 2 and 350 K. These experiments were complemented by low-temperature specific heat and Hall-effect measurements (2–300 K). First-principles calculations were carried out to determine the evolution of the electronic structure as a function of x. Both theoretical and experimental results evidence a progressive evolution, with the Au content, from a metallic-like behavior towards a highly doped semiconducting state which develops around $x = 5.43$. At this concentration, a crossover from n- to p-type conduction occurs, suggesting that the present system satisfies the Zintl–Klemm concept, which predicts a transition at $x = 5.33$. This crossover is traced by Hall-effect data indicating a dominant electronlike response for $x \leqslant 5.43$, which turns into a holelike signal at higher x values. Analysis of the data based on a single-parabolic-band model under the assumption of a single scattering mechanism of the charge carriers proved to adequately describe the transport properties in the compositional range investigated. Interestingly, the temperature dependence of the lattice thermal conductivity is strongly influenced by the Au concentration: the typical behavior of crystalline insulators in the n-type compounds evolves into a glasslike dependence in the p-type samples. The series $Ba_8Au_xSi_{46-x}$ thus provides an excellent testing ground for the interplay between crystal structure, electronic properties, and lattice thermal conductivity in type-I clathrates.

DOI: 10.1103/PhysRevB.84.195137 PACS number(s): 72.15.−v, 82.75.−z

I. INTRODUCTION

Intermetallic clathrates based on a silicon framework and crystallizing in the so-called type-I crystal structure have recently attracted considerable attention due to the occurrence of superconductivity below $T_C = 8$ K in Ba_8Si_{46}.[1,2] Several studies were devoted to better understand the underlying mechanism mediating superconductivity as well as the role played by substitutions on either the Ba or Si sites. These investigations revealed that the thermodynamic properties of the superconducting state can be satisfactorily described within BCS theory and showed a doping-induced decrease of the critical temperature, independent of the substituting element.[2–8]

The cagelike crystal structure together with the large number of possible substitutions also make this family of compounds a prospective area of research for novel thermoelectric materials.[9,10] The thermoelectric efficiency of a material is governed by the dimensionless figure of merit $ZT = \alpha^2 T/\rho\kappa = PT/\kappa$ where α is the thermopower, ρ the electrical resistivity, κ the total thermal conductivity, $P = \alpha^2/\rho$ the power factor, and T the absolute temperature.[11] Band-structure calculations carried out on several $Ba_8M_xSi_{46-x}$ systems revealed that most of the transition metals induce metallic properties preventing the achievement of high ZT values.[7,12] However, some elements, such as Ga, Al, Au, or Ag, were found to induce a metal-insulator transition, offering an experimental phase space to optimize the power factor and thus the ZT values.[13–16] In this regard, maximum ZT of ∼0.75 and ∼0.87 at 1,000 and 870 K, respectively, were reported for the $Ba_8Ga_xSi_{46-x}$ system, where a semiconducting state is expected to develop at $x = 16$.[17–19] These values are comparable to the ones obtained in the single- and polycrystalline Ge-based analog $Ba_8Ga_{16}Ge_{30}$, suggesting that high ZT might be equally achieved in Si-based type-I clathrates.[20,21]

These results thus raise the question whether or not Au substitution in Ba_8Si_{46} may also lead to high thermoelectric efficiency, as recently shown in the isostructural phase $Ba_8Au_xGe_{46-x-y}\square_y$.[22] In the $Ba_8Au_xSi_{46-x}$ system, Jaussaud *et al.*[23] reported that a transition from n- to p-type conduction occurs for Au content falling between $x = 5.43$ and 5.89. In addition, single crystal x-ray diffraction analyses showed that Au atoms are not only located at the 6c site of the framework, as encountered for most of transition-metal-substituted type-I clathrates, but distributed over both the 6c and the 24k sites.[9,23] Hence, extending these measurements to a broader concentration range may provide valuable insights into the evolution of the electronic properties on both the n- and p-type sides and may enable one to better evaluate the thermoelectric potential of this family of compounds.

Here, we report a joint theoretical and experimental study of the low-temperature transport properties of polycrystalline $Ba_8Au_xSi_{46-x}$ in the composition range $4.10 \leqslant x \leqslant 6.10$. Our results confirm a crossover from n- to p-type conduction near $x = 5.43$, thereby offering the possibility to tune the thermoelectric properties on both sides. The dependence upon substitution of several material parameters relevant to the optimization of thermoelectric properties is addressed within a single-parabolic-band model using relations obtained as solutions to the classic Boltzmann transport equations. The intriguing influence of Au substitution on the lattice thermal

conductivity, which evolves from crystallike behavior in the *n*-type samples to glasslike behavior in the *p*-type samples is further discussed in light of prior investigations on Ge- and Sn-based type-I clathrates.

II. EXPERIMENTAL AND COMPUTATIONAL DETAILS

Polycrystalline samples of $Ba_8Au_xSi_{46-x}$ with nominal compositions $0.2 \leqslant x \leqslant 10$ were prepared from crystalline Ba (ChemPur, 99.9%), Au granules (ChemPur, 99.99%), and Si pieces (ChemPur, 99.9999%) in an Ar-filled glove box. Stoichiometric mixtures of the elements were placed in glassy carbon crucibles (Ø = 12 mm, $l = 12$ mm, Sigradur G, HTW) and melted using an induction furnace (5 kW, coil Ø = 40 mm, l = 35 mm, Hüttinger; IR-pyrometer, Maurer). No weight loss was observed during the heating process. The molten samples were then quenched between two steel plates. To improve the chemical homogeneity, the resulting bulk materials were subsequently transferred in glassy carbon crucibles, sealed in tantalum tubes, jacketed in Ar-filled quartz ampoules, and annealed at 900 °C for three weeks. At the end of the annealing process, the reaction ampoules were quenched in water.

The reaction products were characterized by powder x-ray diffraction (PXRD) and microstructure analyses. PXRD data were obtained at room temperature using an x-ray Guinier diffraction technique (Huber G670 camera, Cu-$K\alpha_1$ radiation, $5^\circ \leqslant 2\theta \leqslant 100^\circ$). The reflection positions were determined by profile deconvolution and corrected by LaB_6 [$a = 4.15683(9)$ Å at 295(2) K] as internal standard. The unit cell parameter of clathrate compounds was calculated from a least-square refinement with the WinCSD program package.[24] The Rietveld refinements were performed with the same program on data collected by a STOE STADI P diffractometer [Ge (111) monochromator, Cu-$K\alpha_1$ radiation, zero-background holder, Bragg-Brentano geometry]. Single-crystal x-ray diffraction data were collected with a rotating-anode diffractometer (RIGAKU Spider, Varimax optical system, Ag-$K\alpha$ radiation, $\lambda = 0.56087$ Å). During the data collection, a multiscan absorption correction was applied. Crystal structure determination and refinements were performed with WinCSD. Phase analyses of polished bulk samples were carried out using a Philips XL 30 Scanning Electron Microscopy (SEM) with integrated Energy Dispersive X-ray (EDX) spectrometer. The compositions of the clathrate phase were determined with a Cameca SX 100 Wavelength Dispersive X-ray (WDX) spectrometer using Ba_6Ge_{25}, Au, and NiSi as external standards for the determination of the Ba, Au, and Si content, respectively.

For transport property investigations, bar-shaped samples were cut from the annealed ingots into typical dimensions of $2 \times 2 \times 6$ mm^3 with a diamond-wire saw. Thermoelectric properties, including electrical resistivity, thermopower, and thermal conductivity, were simultaneously measured using the thermal transport option of a physical property measurement system (PPMS, Quantum Design) in the 5–350 K temperature range. Hall-effect measurements were carried out by using an ac transport option of the PPMS between 10 and 300 K and under magnetic fields ranging from −5 to 5 T. A five-point method, using copper wires attached onto the sample with a tiny amount of silver paste, was used. Specific heat measurements under zero magnetic field were performed with a PPMS by a standard relaxation method between 1.9 and 15 K and up to 300 K for selected samples.

First-principles electronic structure calculations were performed using the all-electron, full-potential local orbital method (FPLO).[25] Exchange-correlation effects were taken into account within the local density approximation (LDA) by the Perdew–Wang parameterization.[26] The space group $P1$ (no. 1) was utilized to investigate the band structures and the distribution of Au atoms in $Ba_8Au_xSi_{46-x}$ ($x = 4, 5, 6$). The actual space group $Pm\bar{3}n$ (no. 223) of type-I clathrates could be used only for $x = 6$ where all Au atoms occupy the 6*c* Wyckoff position. Atomic positions were optimized by minimizing forces with a tolerance of 15 meV.Å^{-1}. In addition, the lattice parameters were optimized to accuracy better than 0.01 Å.

III. RESULTS AND DISCUSSION

A. Chemical and structural characterizations

Clathrate samples with nominal compositions $Ba_8Au_xSi_{46-x}$ ($0.2 \leqslant x \leqslant 10$) were characterized after steel-quenching and annealing at 900 °C for 3 weeks. The lowest Au content of $x \approx 2.2$ was obtained after steel-quenching a sample with the nominal composition $Ba_8Au_{0.2}Si_{45.8}$ [Figs. 1(a) and 1(b)]. Besides the clathrate phase, this sample contains large amounts of $BaSi_2$ and α-Si (in total >90 wt.%). Compounds with higher Au content were obtained after annealing at 900 °C for 3 weeks. After annealing the $Ba_8Au_{0.2}Si_{45.8}$ sample, the lattice parameter was refined to be $a = 10.3915(4)$ Å, which is close to the value of 10.3894(1) Å for the composition $x = 3.6$ (Table I). For $x = 3.0$, the amount of secondary phases ($BaSi_2$ and α-Si) decreases after annealing at 900 °C [Fig. 1(c)], and quasisingle clathrate phase was obtained in the composition range $4.0 \leqslant x \leqslant 6.0$ [Figs. 1(d)–1(g), Table I]. For these samples, the size of the clathrate grains was estimated from SEM images to be larger than 200 μm. The impurity phase α-Si precipitates within the clathrate grains but not at the grain boundaries. In the present series of samples, the highest Au content was found to be $x = 6.10$, and a further increase in x, e.g. $Ba_8Au_{10}Si_{36}$, leads to a large amount of Au-rich secondary phase as observed by PXRD and microstructural analysis [Fig. 1(h), Table I].

PXRD patterns of all the clathrate compounds could be indexed with a primitive cubic lattice in agreement with the space group $Pm\bar{3}n$ (Fig. 2). No supercell reflections indicative of an ordered arrangement of Au atoms or vacancies in the Si framework could be identified. The crystal structure of type-I clathrates comprises two pentagonal dodecahedra and six tetrakaidecahedra per unit cell (Fig. 3).[9,27] These polyhedra encapsulate the guest atoms (Ba), located at the 2*a* (Ba1) and 6*d* (Ba2) sites. The framework of clathrate-I silicides is built up by atoms located at three distinct crystallographic sites, 6*c* (Si1), 16*i* (Si2), and 24*k* (Si3). Considering that these positions are fully occupied, all Si atoms are four bonded. However, only the bond angles at the Si2 position are close to the ideal tetrahedral angle of 109.5°, as expected for a network of Si atoms exhibiting sp^3 hybridization. The bond angles for atoms at Si1 and Si3 sites are close to 120°. Si1 atoms join two hexagons of the tetrakaidecahedra with

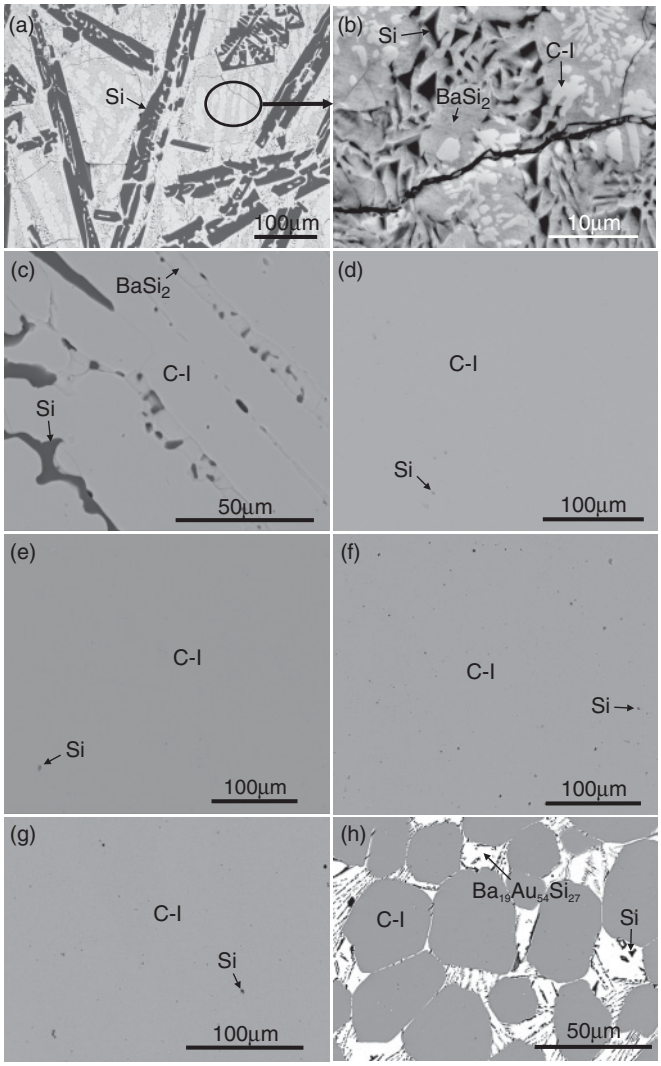

FIG. 1. SEM images of the samples with nominal compositions (a) and (b) $Ba_8Au_{0.2}Si_{45.8}$ (c) $Ba_8Au_3Si_{43}$, (d) $Ba_8Au_4Si_{42}$, (e) $Ba_8Au_5Si_{41}$, (f) $Ba_8Au_{5.6}Si_{40.4}$, (g) $Ba_8Au_6Si_{40}$, and (h) $Ba_8Au_{10}Si_{36}$. Except for (b), which is in secondary-electron contrast, all other images were obtained in backscattered electron contrast. The different phases are shown by arrows, C-I referring to the clathrate-I phase.

$\sim$120° bond angles so that the coordination environment is especially unfavorable for four-bonded Si atoms. Therefore, substituting atoms (in particular transition-metal atoms) or vacancies preferentially occupy the 6*c* site. However, the atoms substituting the framework element can also be located at the 24*k* site and even at the 16*i* site for some elements such as Ga or Al.[9] Boron represents a remarkable exception to this behavior since this element preferentially occupies the 16*i* site in $K_7B_7Si_{39}$.[28]

First single-crystal x-ray diffraction analyses on type-I clathrates in the Ba-Au-Si system were performed by Cordier and Woll on $Ba_8Au_6Si_{40}$.[29] In the reported crystal structure, all Ba positions (2*a* and 6*d*, see Fig. 3) were found to be fully occupied, and the Au atoms were refined to be only at the 6*c* site, leaving the 24*k* and 16*i* sites solely occupied by Si atoms. Recently, single-crystal x-ray diffraction analyses

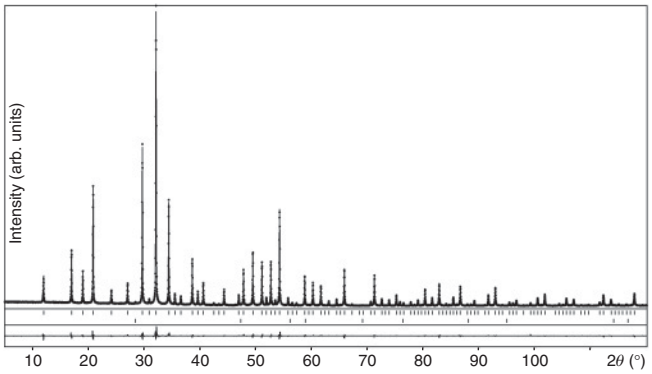

FIG. 2. Powder x-ray diffraction pattern of a sample with nominal composition $Ba_8Au_6Si_{40}$ (dotted line). The calculated profile after Rietveld refinement (solid line) and difference curve (below) are shown. Upper and lower ticks mark the calculated reflection positions of the clathrate phase and α-Si, respectively.

were carried out by Jaussaud *et al.*[23] on two compounds with the compositions $Ba_8Au_{5.43}Si_{40.57}$ and $Ba_8Au_{5.89}Si_{40.11}$. According to their refinements, the Ba sites were fully occupied, in agreement with the previous investigation. However, the Au atoms were found to be distributed on both the 6*c* and 24*k* sites, while the 16*i* site was fully occupied by Si atoms. Though Au preferentially occupies the 6*c* site (5.14 and 5.56 Au atoms per unit cell for $Ba_8Au_{5.43}Si_{40.57}$ and $Ba_8Au_{5.89}Si_{40.11}$, respectively), a small concentration located at the 24*k* site could be refined (0.29 and 0.33 Au atoms per unit cell, respectively). Their refinements indicated no vacancies in the crystal structure of both compounds. For our single-crystal x-ray diffraction experiment, a crystal was picked from a sample with the composition $Ba_{8.00(2)}Au_{6.10(2)}Si_{38.97(4)}$. The refinement results are in accordance with the published single-crystal data.[23] Besides Ba sites being fully occupied, Au atoms were found to mainly occupy the 6*c* site, and a small amount ($\sim$0.5 Au atoms) was refined at the 24*k* site. The 16*i* site was fully occupied by Si atoms. Moreover, the presence of a

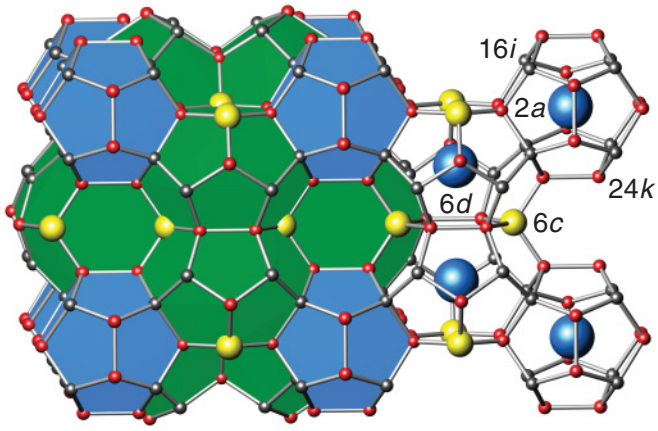

FIG. 3. (Color online) Crystal structure of the type-I clathrate $Ba_8Au_xSi_{46-x}$. The pentagon dodecahedra and tetrakaidecahedra are shown in blue (medium gray) and green (gray), respectively. The framework atoms are located at the 6*c* (yellow/light gray), 16*i* (gray), and 24*k* (red/dark gray) sites, while the Ba atoms are located at the 2*a* and 6*d* (blue/medium gray) sites.

TABLE I. Determined compositions, nature of the secondary phases, and lattice parameter (a) of the $Ba_8Au_xSi_{46-x}$ samples. While the Au content of the steel-quenched sample with nominal composition $Ba_8Au_{0.2}Si_{45.8}$ was determined from a linear fit of the lattice parameter data (see Fig. 4), all the other samples were annealed at 900 °C and the compositions obtained by WDXS.

Nominal composition	Determined composition	Secondary phases	a (Å)
$Ba_8Au_{0.2}Si_{45.8}$	$Ba_8Au_{2.2}Si_{43.8}$	$BaSi_2 + \alpha$-Si	10.3673(6)
$Ba_8Au_3Si_{43}$	$Ba_{8.00(4)}Au_{3.63(2)}Si_{41.11(5)}$	$BaSi_2 + \alpha$-Si	10.3894(1)
$Ba_8Au_4Si_{42}$	$Ba_{8.00(3)}Au_{4.10(5)}Si_{40.84(5)}$	α-Si	10.39768(8)
$Ba_8Au_{4.75}Si_{41.25}$	$Ba_{8.00(2)}Au_{4.85(2)}Si_{39.72(4)}$	α-Si	10.4084(1)
$Ba_8Au_5Si_{41}$	$Ba_{8.00(2)}Au_{5.10(11)}Si_{39.88(11)}$	α-Si	10.41260(8)
$Ba_8Au_{5.15}Si_{40.85}$	$Ba_{8.00(2)}Au_{5.14(2)}Si_{39.51(2)}$	α-Si	10.41473(8)
$Ba_8Au_{5.30}Si_{40.70}$	$Ba_{8.00(3)}Au_{5.43(5)}Si_{39.76(6)}$	α-Si	10.41615(9)
$Ba_8Au_{5.45}Si_{40.55}$	$Ba_{8.00(2)}Au_{5.59(2)}Si_{39.01(3)}$	α-Si	10.41747(8)
$Ba_8Au_{5.60}Si_{40.40}$	$Ba_{8.00(3)}Au_{5.76(2)}Si_{39.21(4)}$	α-Si	10.41761(9)
$Ba_8Au_6Si_{40}$	$Ba_{8.00(2)}Au_{6.10(2)}Si_{38.97(4)}$	α-Si	10.41767(9)
$Ba_8Au_{10}Si_{36}$	$Ba_{8.00(2)}Au_{6.01(2)}Si_{38.90(3)}$	$Ba_{19}Au_{54}Si_{27} + \alpha$-Si	10.4174(1)

small amount of vacancies ($\leqslant$0.3 per formula unit) at the 6c site cannot be ruled out. Rietveld refinements performed on PXRD data for different clathrate compositions ($x = 4.0$, 5.0, and 6.0) agree with our data and the published single-crystal data.[23] The occupation of different crystallographic sites by transition metal atoms is not confined to the Ba-Au-Si system, and Pt and Pd were also found to partially occupy the 24k sites in $Ba_8Pt_xSi_{46-x}$ and $Ba_8Pd_xSi_{46-x}$.[30]

Figure 4 shows the variations in the lattice parameter a with the actual Au content of the samples investigated. Here, a increases linearly up to $x = 5.59$ before exhibiting quasiconstant values up to $x = 6.10$. It is worth mentioning that the reported lattice parameter for $Ba_8Au_{5.43}Si_{40.57}$ [a = 10.414(1) Å][23] is close to that obtained here for the x = 5.14 sample [a = 10.41473(8) Å]. As already suggested by these authors, this result points to a lower actual Au content than the claimed composition, thereby explaining the n-type behavior observed for this sample, which was at odds with

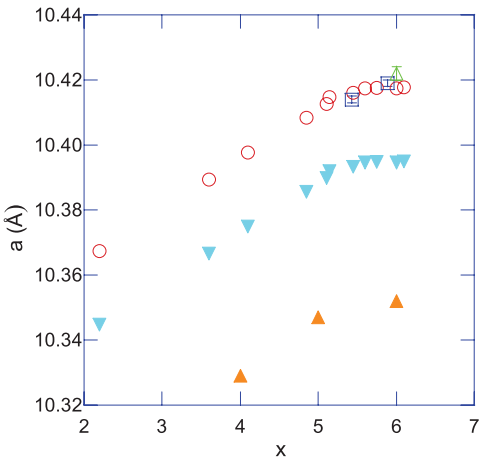

FIG. 4. (Color online) Lattice parameter a of $Ba_8Au_xSi_{46-x}$ as a function of the actual Au content: (○) the present series of samples, (▽) extrapolated to $T = 0$ K, (□) reported by Jaussaud *et al.* (Ref. 23), (△) by Cordier *et al.* (Ref. 29), and (▲) derived from our band structure calculations. For our samples, the error bars related to the estimated standard deviations of the lattice parameters are smaller than the size of the symbols used.

the p-type conduction expected for $x = 5.43$, according to the Zintl–Klemm concept. The expansion of the lattice parameter with x is consistent with an increase of the gold content at the 6c site due to the larger size of the Au atoms with respect to Si atoms. This is further confirmed by the Au1-Si3 interatomic distances [$d_{\text{Au1-Si3}} \approx 2.44$ Å, $a = 10.414$ (1) Å], which are longer than the Si1-Si3 bond length in Ba_8Si_{46} [$d_{\text{Si1-Si3}} \approx$ 2.40 Å, $a = 10.328(2)$ Å].[1,31] As mentioned above, the Au atoms also occupy partially the 24k site at high x values.[23] However, whether a small concentration of Au located at this site can explain the saturation of the lattice parameter above $x = 5.59$ is not yet clear. In addition, as shown by our band structure calculations (Section B), the variations in a with x can be derived assuming that Au only substitutes Si on the 6c site. The expansion of the crystal lattice upon alloying with Au is not fully understood and requires further investigations.

B. First-principles calculations

1. *Total energy calculations*

The clathrate $Ba_8Au_xSi_{46-x}$ ($4 \leqslant x \leqslant 6$) exhibits an inherent chemical disorder due to Au and Si atoms sharing at least one Wyckoff position. One way of treating this disorder in first-principles calculations is using ordered models. We have chosen to work with the 54-atom unit cell with space group $P1$ (no. 1). The cases $x = 4$ and 5 involve Au-Si disorder only at the 6c Wyckoff position of the space group $Pm\bar{3}n$, while for $x = 6$, refinements on single-crystal data show that Au is distributed over both the 6c and 24k sites.

In the crystal structure of type-I clathrates, two 6c sites and four 24k sites form a planar hexagon, and each hexagon is connected to another perpendicular one at a 6c site (Fig. 3).[9,10,31–33] Hence, each atom at the 6c site has four atoms at the 24k site as the nearest neighbors. The two 6c sites belonging to a particular hexagon lie on a line parallel to one of the crystallographic axes [100], [010], or [001]. Therefore, two distinct ordered models are possible for the clathrate $Ba_8Au_4Si_{42}$ in the 54-atom unit cell: the 6c sites of each hexagon contain atoms of the same element (Au-Au and Si-Si pairs), or two of the three hexagons have mixed Au-Si pairs at their 6c sites. Total energy calculations favor the mixed-pair model by 1.76 meV per atom. The fully

optimized structure of this model has a lattice parameter of 10.329 Å, which represents a smaller unit cell volume (2.0%) in comparison to experiment, a deviation well within the typical LDA values. In the case of $Ba_8Au_5Si_{41}$, there is only one possible configuration with Au atoms placed at five of the 6*c* sites. Full optimization yields a theoretical volume smaller than the experimental one by 1.9% (the theoretical lattice parameter is 10.347 Å). $Ba_8Au_6Si_{40}$ is the most complex case since the disorder is found to involve two Wyckoff positions. We have considered the following configurations in our total-energy explorations: (i) all six Au atoms at the 6*c* sites; (ii) five Au atoms at 6*c* and one at a 24*k* site, which is one of the nearest neighbors of the Si atom at the remaining 6*c* site; (iii) five Au atoms at 6*c* and one at a 24*k* site, which is a nearest neighbor of one of the Au atoms at 6*c*; (iv) five Au atoms at 6*c* and one at a 16*i* site. Though the last two cases can be further divided into two distinct configurations, these models were found to be energetically unfavorable and will not be discussed further in the following analysis. The configuration where all 6*c* sites are occupied by Au atoms has the lowest total energy. If this energy is taken as zero, then the energies of the other configurations are, respectively, 7.0, 26.6, and 17.2 meV per atom. As expected, Au-Au contacts with a distance typical of a covalently bonded Si framework are energetically unfavorable, therefore preventing the clustering of Au atoms in the clathrate crystal structure. A simple statistical mechanical model, which takes into account configurational entropy,[34] predicts a site occupancy factor (for Au at 24*k*) of 0.0065 at $T = 900$ K, roughly half of the experimental values reported at room temperature.[23] This discrepancy may have two sources: (i) neglect of entropy contributions due to phonons, (ii) since placing one Au atom at a 24*k* site largely exceeds the experimentally determined occupancies (0.2–0.3 Au atoms at 24*k* sites), our calculations based on the 54-atom cell may have given a much higher total energy. Nevertheless, we optimized the crystal structures of both models (i) and (ii). The equilibrium lattice parameters are found to be practically the same within the numerical accuracy, 10.352 Å (the theoretical lattice volume is smaller than the experimental one by 1.9%). This result implies that, once five out of six 6*c* sites are occupied by Au atoms, then the equilibrium volume is not affected by whether the sixth Au atom is located at the remaining 6*c* site or at a 24*k* neighbor of the Si atom at 6*c*.

A comparison of the theoretical lattice parameters for $x = 4$, 5, and 6 with their experimental counterparts, extrapolated to $T = 0$ K using the thermal expansion coefficient measured by Falmbigl *et al.*,[35] reveals that theoretical values are smaller by almost the same factor, and thus both sets of data convey the same behavior (Fig. 4). The slopes derived from first-principles data are 0.018 Å per x for $4 \leqslant x \leqslant 5$, and 0.005 Å per x for $5 \leqslant x \leqslant 6$.

2. *Electronic band structure*

Both previous and present experimental studies point to the existence of a metal-insulator transition in $Ba_8Au_xE_{46-x}$ (E = Si, Ge) around $x = 16/3 \sim 5.33$.[22,23] The justification for this observation relies on the assumption that Au atoms with an electronic configuration s^1d^{10} located at 6*c* sites need three extra electrons to form two-center two-electron bonds with their four neighboring E atoms, the eight Ba atoms providing 16 electrons in total. An examination of the total density of states (DOS) computed for $x = 4$, 5, and 6 (Fig. 5) reveals a theoretical explanation for the observed transition. For $x = 6$, a narrow energy gap of width ~0.08 eV is located ~0.15 eV above the Fermi energy (set to 0 eV), which suggests *p*-type electrical conduction. On the other hand, in the case of $x = 5$, the DOS nearly vanishes at ~0.14 eV below the Fermi energy, indicating *n*-type electrical conduction. Clearly, an *n*-type-*p*-type crossover occurs between $x = 5$ and 6. It is likely that the gap in the $x = 6$ case and the dip observed at $E = -0.14$ eV for $x = 5$ correspond to a semiconducting composition. This is further supported by the integration of the DOS between 0 and 0.15 eV for $x = 6$ and between −0.14 and 0 eV for $x = 5$, which gives exactly two and one electrons, respectively. In order to understand these values, let us consider the following idealized situation: assuming one and four valence electrons for Au and Si, respectively, one obtains a difference of three electrons between the $x = 5$ and $x = 6$ cases. If we take $x = 6$ as reference and start decreasing the Au content, the electron number will increase by two at exactly $x = 16/3 \sim 5.33$. Equivalently, if $x = 5$ is taken as reference and we start increasing the Au content, the decrease in electron number will reach one, again at exactly $x = 16/3$. Therefore, the values obtained from integrated DOS coincide perfectly with the values expected from idealized valence electron numbers. As far as electronic states are concerned, the composition corresponding to $x = 16/3$ is predicted to be a semiconductor, in agreement with our experimental results (see below).

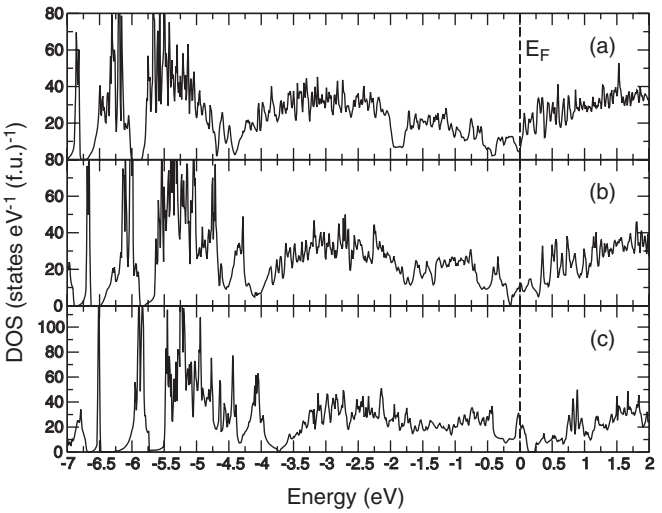

FIG. 5. Energy dependence of the total density of states near the Fermi level of $Ba_8Au_xSi_{46-x}$ for (a) $x = 4$, (b) $x = 5$, and (c) $x = 6$. The vertical dashed line at 0 eV stands for the Fermi level.

The total DOS shown in Fig. 5 and the dispersion curves in Fig. 6 were computed using the experimental lattice parameters and optimized atomic coordinates. The $x = 4$ and 6 cases are related to the models which have the lowest total energy. The occupancies of the relevant states as obtained from projected DOS are independent of the Au content. Au 5*d*, 6*s*, and 6*p* states have approximately 9.40, 0.80, and 0.65 electrons, respectively. The 5*d* states of Ba1 and Ba2 atoms have 0.8

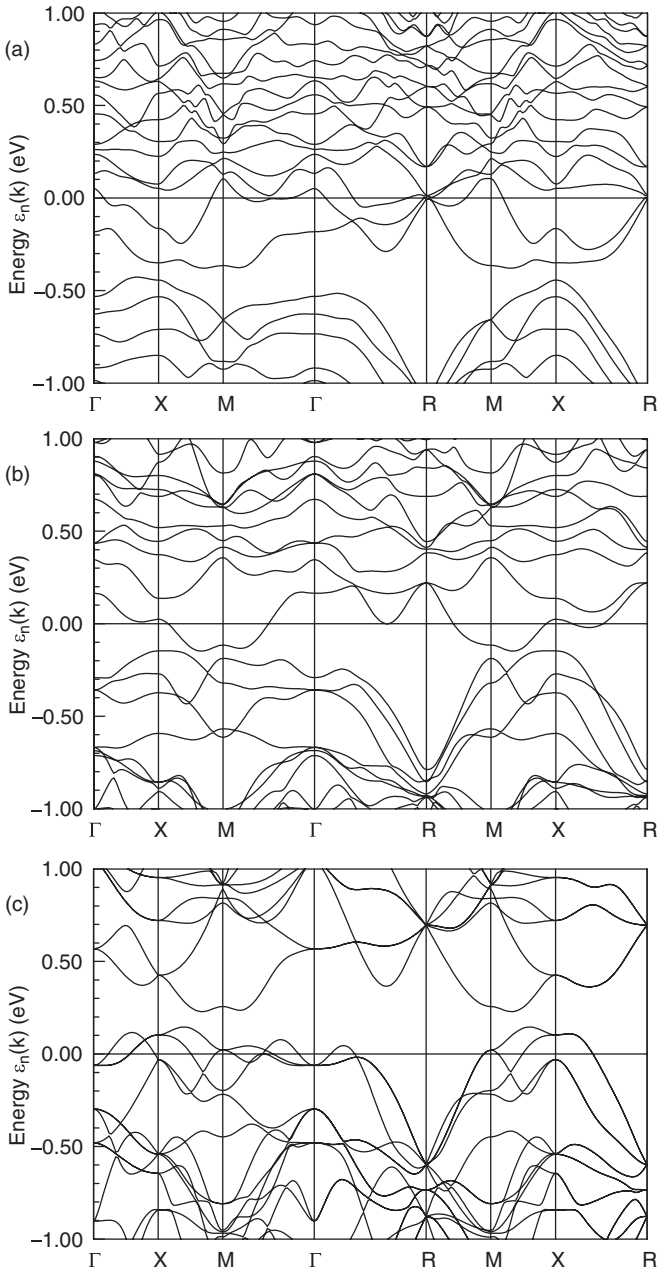

FIG. 6. Dispersion curves along high-symmetry directions near the Fermi level of $Ba_8Au_xSi_{46-x}$ for (a) $x = 4$, (b) $x = 5$, and (c) $x = 6$.

and 0.6 electrons, respectively. Remarkably, these values for Ba are essentially similar to those found in the $Ba_8Ni_xSi_{46-x}$ system.[12] The values of the DOS at the Fermi energy, $N(E_F)$, are 5.24, 11.95, and 25.23 states eV^{-1} per unit cell for $x = 4$, 5, and 6, respectively. However, the number of bands crossing E_F seems to better reflect the proximity of the $x = 5$ compound to a semiconducting state since two, one, and three bands intersect E_F for $x = 4$, 5, and 6, respectively (Fig. 6).

The facts that the calculated Au $5d$ occupancies are very high and the integrated DOS analysis gives a picture consistent with the idealized Au electronic configuration of s^1d^{10} suggest that Au $5d$ orbitals are only weakly hybridized with the orbitals of the neighboring atoms. Hence, the $5d$ states of Au atoms give rise to narrow and sharp features indicative of weakly dispersing bands. The total DOS is dominated by the Au $5d$ contributions in the energy ranges (−7.0, −4.4) eV, (−6.75, −4.0) eV and (−6.6, −3.75) eV for $x = 4$, 5, and 6, respectively. Above these specified energy regions and up to the Fermi energy, the Si $3p$ contributions become more dominant. Interestingly, one can notice rigid-band behavior in this region in sharp contrast with the $Ba_8Ni_xSi_{46-x}$ system for $0 \leqslant x \leqslant 4$, where nonrigid-band evolution was observed.[12] This rigidlike behavior is further shown by the electron energy bands in the vicinity of the Fermi energy. As can be seen in Fig. 6, E_F shifts down by approximately 0.3 eV on going from $x = 4$ to $x = 5$, and from $x = 5$ to $x = 6$ with only small variations in the overall shape of the bands.

C. Electronic properties

Figure 7 shows the temperature dependence of the electrical resistivity. No superconducting transition was observed down to 1.9 K, suggesting a substantial weakening of the electron-phonon coupling strength upon alloying. Except for the $x = 5.43$ compound, which shows semiconducting behavior, all the samples exhibit a metallic behavior in the whole temperature range. For $x = 4.10$, the measured values are low and characteristic of a metallic system (Table II). Increasing the Au content then leads to higher resistivity values, which remain practically unchanged for $4.85 \leqslant x \leqslant 5.14$. At higher Au contents ($x > 5.43$), ρ significantly drops and decreases with x, the lowest values being achieved at $x = 6.10$. As we shall see below, the variations in ρ are consistent with a crossover from an n- to a p-type metal near the theoretical concentration $x = 5.33$ via a semiconducting state ($x = 5.43$). Within this scenario, the variations in the electrical resistivity should mainly reflect the variations in the charge carrier concentration.

We carried out measurements of the Hall coefficient over the 10–300 K temperature range in order to determine the charge carrier concentrations and mobility. Figures 8(a) and 8(b) show the transverse Hall resistivity ρ_{xy} as a function of the

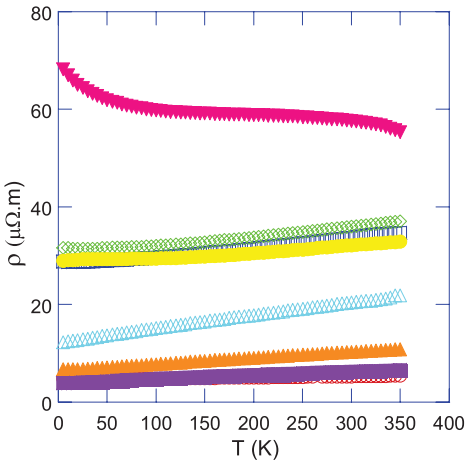

FIG. 7. (Color online) Temperature dependence of the electrical resistivity ρ of the $Ba_8Au_xSi_{46-x}$ samples for (○) $x = 4.10$, (□) $x = 4.85$, (◊) $x = 5.10$, (●) $x = 5.14$, (▼) $x = 5.43$, (△) $x = 5.59$, (▲) $x = 5.76$, and (■) $x = 6.10$.

TABLE II. Room temperature values of the electron (n, for $4.10 \leqslant x \leqslant 5.14$) and hole ($p$, for $5.43 \leqslant x \leqslant 6.10$) concentrations, Seebeck coefficient (α), and electrical resistivity (ρ) of the different $Ba_8Au_xSi_{46-x}$ compounds studied. The total thermal conductivity (κ) values are given at 200 K due to the radiative contribution responsible for the slight upturns observed above this temperature.

Au content from WDXS	n/p (10^{21} cm^{-3})	α (μV.K^{-1})	ρ ($\mu\Omega$.m)	κ (W.m^{-1}.K^{-1})
4.10	6.5	−9.1	5.3	3.6
4.85	4.1	−32.6	33.7	2.3
5.10	1.9	−65.4	36.0	2.3
5.14	0.8	−90.9	32.1	2.2
5.43	0.8	107.2	57.6	1.9
5.59	1.5	107.6	20.4	2.2
5.76	3.1	64.1	10.3	1.6
6.10	7.2	38.9	6.2	1.7

magnetic field $\mu_0 H$ at selected temperatures for the illustrative $x = 5.10$ and 5.76 samples. In the whole temperature and field ranges covered by these experiments and regardless of the Au content, the initial Hall coefficient $R_H = \frac{d\rho_{xy}}{dH}|_{H=0}$ is well defined as no departure from linearity is observed in $\rho_{xy}(\mu_0 H)$, suggesting the absence of multiband conduction. The negative slope observed in the $x = 5.10$ sample turns into a positive one in $x = 5.76$, indicating a transition from an electron-dominated transport response to hole-dominated transport with increasing x. These results thus show that

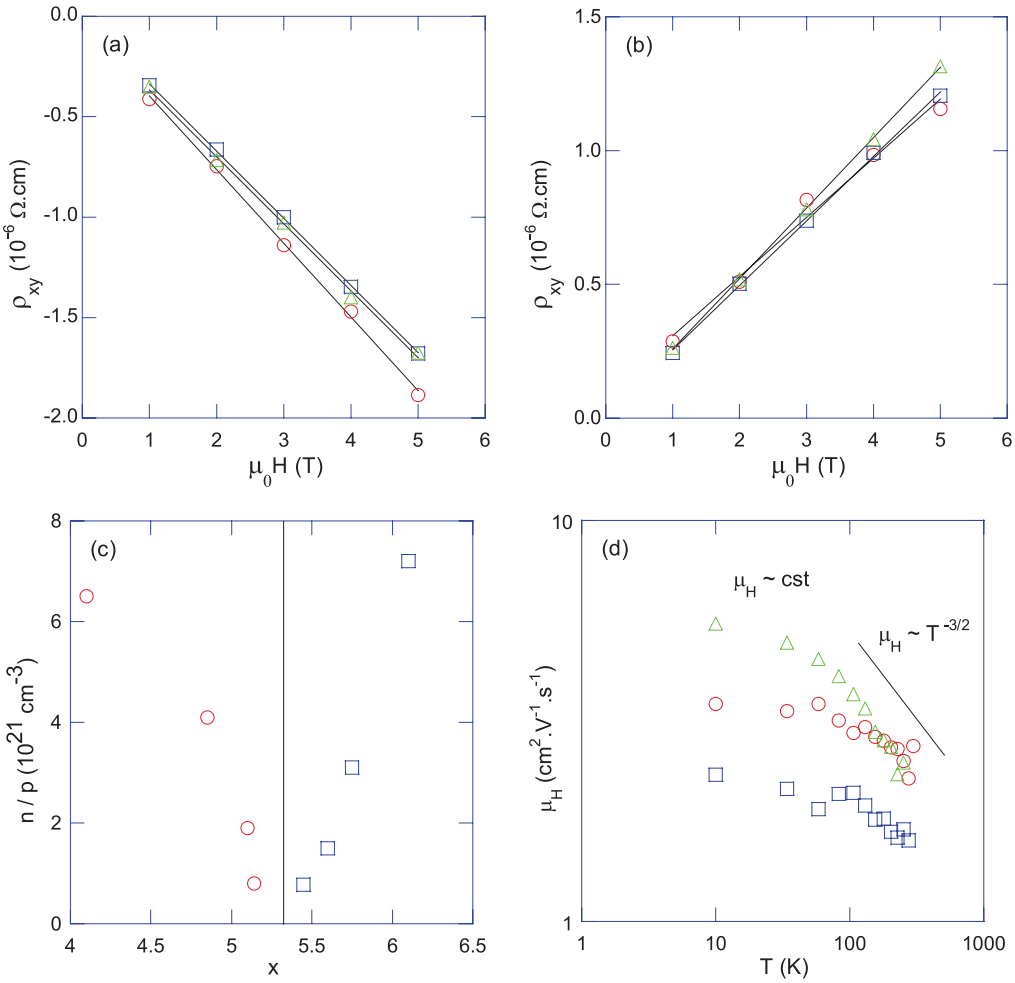

FIG. 8. (Color online) Transverse Hall resistivity ρ_{xy} as a function of the magnetic field $\mu_0 H$ of $Ba_8Au_xSi_{46-x}$ for (a) $x = 5.10$ and (b) $x = 5.76$ measured at (○) 275 K, (□) 105 K, and (△) 35 K and (○) 200 K, (□) 155 K, and (△) 10 K, respectively. The solid black lines stand for the best fit to the data highlighting the linearity of the $\rho_{xy}(\mu_0 H)$ data. (c) (○) Electron and (□) hole concentrations as a function of the Au content. The solid black line delineates the n- and p-type regions according to the Zintl concept ($x = 5.33$). (d) Temperature dependence of the Hall mobility μ_H of the $x = 5.14$, 5.59, and 6.10 samples.

an n-type-p-type crossover occurs, as suggested by our band structure calculations (Section B). Within a single-band picture, the Hall coefficient R_H is related to the electron and hole concentrations n and p, respectively, through the relations $n = -1/R_H e$ and $p = 1/R_H$e, where e is the elementary charge. As shown in Fig. 8(c), the carrier concentration first decreases with x before increasing from $x = 5.43$ up to 6.10, confirming the evolution of this system from n- to p-type metallic states via a semiconducting region near $x = 5.33$.

The Hall mobility of the charge carriers $\mu_H = R_H/\rho$ remains low across the entire Au concentration range, of the order of a few $cm^2.V^{-1}.s^{-1}$, as shown in Fig. 8(d), which depicts the temperature dependence of μ_H for the illustrative $x = 5.14$, 5.59, and 6.10 samples. Below 50 K, μ_H is quasiconstant, while above this temperature, the mobility of the charge carriers decreases following approximately a $T^{-1.5}$ law. The temperature dependence of μ_H can be usually explained by the conventional theory of itinerant electron or hole conduction involving multiple-scattering sources. In this model, μ_H can be limited by ionized-impurity, acoustic-phonon, or neutral-impurity scattering, which gives rise to temperature dependences governed by simple power laws, i.e. T^s with $s = 3/2, -3/2$, and 0, respectively. The observed temperature dependence thus points to neutral-impurity scattering dominating below 50 K and acoustic phonon scattering above this temperature.

The temperature dependence of the thermopower is shown in Fig. 9. Below $x = 5.14$, α is negative, indicative of electrons as the dominant charge carriers. With increasing temperature, a linear variation can be observed in the whole temperature range for the $x = 4.10$ and 4.85 compounds, reflecting a diffusive regime. A nonlinear T dependence of the thermopower at low temperatures suggests an evolution from a metallic state at low Au contents ($x = 4.10$ and 4.85) towards highly doped semiconductors for $x = 5.10$ and 5.14. Further addition of Au results in a crossover from n- to p-type conduction, as revealed by positive thermopower values, in agreement with the Hall-effect data. The observed transition occurs at a composition falling between $x = 5.14$ and $x = 5.43$ and thus appears to be

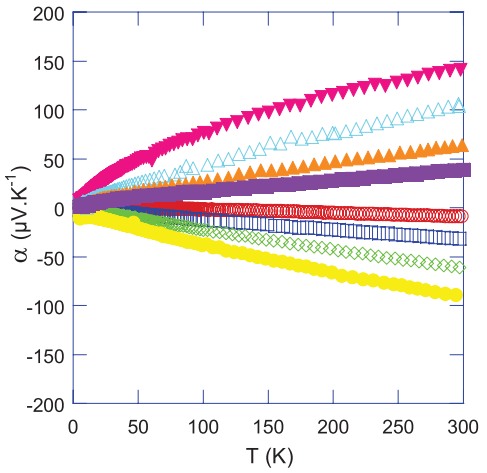

FIG. 9. (Color online) Temperature dependence of the thermopower α of the $Ba_8Au_xSi_{46-x}$ samples for (○) $x = 4.10$, (□) $x = 4.85$, (◇) $x = 5.10$, (●) $x = 5.14$, (▼) $x = 5.43$, (△) $x = 5.59$, (▲) $x = 5.76$, and (■) $x = 6.10$.

consistent with the idea that the Au atoms exhibit a valence state close to Au^+ (s^1d^{10} configuration) in these materials. Increasing the Au content to $x = 5.59$ and 6.10 results in a decrease in the magnitude of $\alpha(T)$, which recovers a linear temperature dependence. This indicates thermal diffusion of the charge carriers, as expected in a metallic state. The overall dependence on x is consistent with the scenario revealed by our first-principles calculations, whereby the Fermi level lies within the conduction bands at low x values (n type), then shifts towards the band edge as x increases and finally crosses the band gap to be located in the valence bands (p type). As x approaches 6.10, the Fermi level moves deeper inside the valence bands, resulting in a more pronounced metallic character.

The $Ba_8Au_xSi_{46-x}$ samples display trends typical of heavily doped semiconductors when x approaches 5.33 from both the n- and p-type sides. The evolution from a metallic to a highly doped regime can be traced by the variations in the position of the Fermi level with respect to the band gap. Combining the thermopower and the Hall-effect data (Table II), the position of the Fermi level can be inferred along with the effective mass of the charge carriers. Within a single-parabolic-band model, the thermopower and carrier concentration can be expressed as[36]

$$\alpha = -\frac{k_B}{e}\left[\frac{(2+\lambda)F_{1+\lambda}(\eta)}{(1+\lambda)F_\lambda(\eta)} - \eta\right] \quad (1)$$

$$p \text{ or } n = \frac{4}{\sqrt{\pi}}\left(\frac{2\pi m^* k_B T}{h^2}\right)^{\frac{3}{2}} F_{\frac{1}{2}}(\eta) \quad (2)$$

where h is the Planck constant, k_B the Boltzmann constant, m^* the effective mass of the charge carriers, λ a scattering constant related to the energy dependence of the electronic scattering mechanism, and F_i the Fermi integral of order i defined as $F_i(\eta) = \int_0^\infty \frac{\xi^i d\xi}{1+\exp[\xi-\eta]}$ where ξ is the reduced energy of the charge carriers and η the reduced Fermi level defined as $\eta = E_F/k_BT$. Assuming that this model can be extended across the Au concentration range between $x = 4.85$ and $x = 6.10$, we can derive m^* and η from Eqs. (1) and (2). Here, we further assume that, near room temperature, acoustic-phonon scattering is the dominant scattering mechanism of the charge carriers for which $\lambda = 0$. The obtained values, listed in Table III, indicate that the effective mass shows only little variations with the Au content on each side, supporting a rigid-band picture unveiled by our band structure calculations. This result also indicates that a single-parabolic-band model describes the conduction

TABLE III. Effective masses (m^*/m_0), reduced Fermi level (η), and Lorenz number (L) estimated at 300 K using Eqs. (1), (2) and (4).

Au content from WDXS	m^*/m_0	η	L ($\times 10^{-8}$ $V^2.K^{-2}$)
4.85	4.1	8.7	2.34
5.10	4.9	4.2	2.11
5.14	3.9	2.8	1.96
5.43	4.7	2.2	1.88
5.59	7.2	2.2	1.88
5.76	6.7	4.3	2.12
6.10	7.1	7.3	2.30

and valence band edges reasonably well. However, crossing the n-type-p-type border leads to a significant change in m^*, which becomes higher in the p-type samples. This change is consistent with the shape of the valence bands, which are flatter than the conduction bands (see Fig. 6). These enhanced values are likely to explain the higher magnitude of α observed in the p-type samples at similar carrier concentration levels (see Table II). In addition, the reduced Fermi level clearly decreases as the Au content increases before increasing again when the conduction switched to p type, in agreement with progressive metal-insulator transitions in both the n- and p-type regions.

D. Thermal properties

Figure 10 shows the temperature dependence of the specific heat, $C_p(T)$, between 1.9 and 300 K for the illustrative $x = 4.85$ and 5.59 samples. Interestingly, as already observed in the isostructural $Ba_8Ga_{16}Ge_{30}$ compound,[20] the $C_p(T)$ values do not reach the Dulong–Petit value near 300 K. This approximation, which is usually used to estimate $C_p(T)$ at high temperatures, thus overestimates the experimental value near and above 300 K.

The specific heat data in the low-temperature regions were fitted using the conventional Fermi-liquid relation $C_p/T = \gamma + \beta T^2$ where γ is the Sommerfeld coefficient reflecting the electronic contribution and βT^2 the phononic contribution. The inferred values of γ and β are listed in Table IV. The variation in γ with x (Fig. 11) shows that γ decreases as the Au content approaches the $x = 5.33$ concentration before following a quasilinear increase up to $x = 6.10$. This variation backs up the trend uncovered by the thermopower data and shows that $N(E_F)$ eventually vanishes at a concentration in the vicinity of $x = 5.33$, for which pure semiconducting behavior is expected. As can be observed, the agreement between the γ values calculated within the FPLO method and the experimental ones is good except for the $x = 4$ compound for which the FPLO value is appreciably smaller. Since such a large enhancement of the Sommerfeld coefficient due to electron-phonon interactions is highly unlikely, the source of the discrepancy probably lies in the ordered crystal structure used in the FPLO calculations to model the $x = 4$ case. Models based on larger supercells may have lower total energies but somewhat higher $N(E_F)$ values.

The β values enable us to extract the Debye temperatures, θ_D, via the relation $\theta_D = [(12\pi^4 RN)/(5\beta)]^{1/3}$ where R is the gas constant and N the number of atoms per formula unit. The θ_D values obtained by using the total number of atoms derived from WDXS experiments are summarized in Table IV. As shown in Fig. 12(a), the addition of Au does not markedly influence θ_D, which remains quasiconstant below $x = 4.85$. This suggests a minimal impact of Au on the phonon spectrum in this composition range. Above this value, however, θ_D slightly decreases in a quasilinear way up to $x = 6.10$. We surmise that a progressive increase in the concentration of Au on the 24k site might have a more pronounced influence on

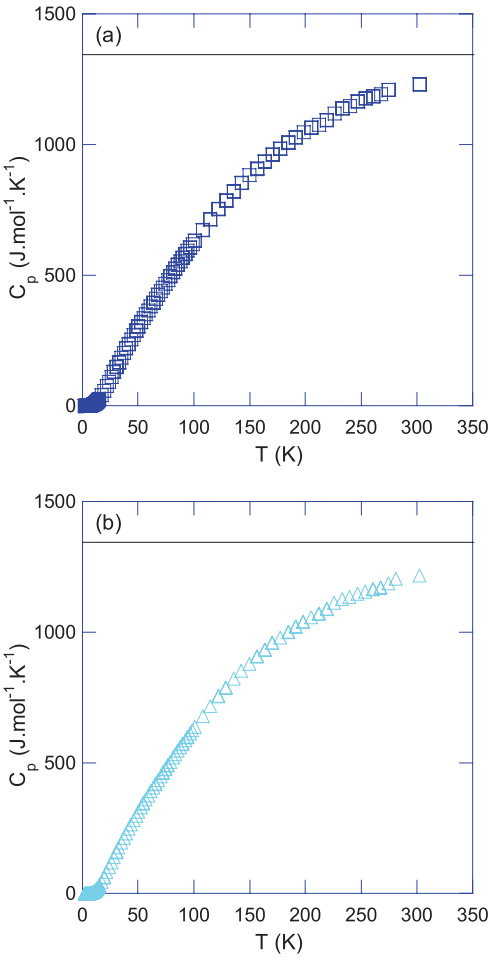

FIG. 10. (Color online) Temperature dependence of the specific heat C_p of the (a) $x = 4.10$ and (b) $x = 6.10$ samples. The black solid line stands for the value expected from the Dulong–Petit law.

TABLE IV. Values of the γ and β parameters inferred from low-temperature specific heat analyses. The experimental and theoretical total DOS values $N(E_F)_{\text{exp}}$ and $N(E_F)_{\text{FPLO}}$ together with the Debye temperatures θ_D derived from the β parameters are also given.

Au content from WDXS	γ (mJ.mol^{-1}.K^{-2})	β (mJ.mol^{-1}.K^{-4})	$N(E_F)_{\text{exp}}$ (states.Ry^{-1}f.u.$^{-1}$)	$N(E_F)_{\text{FPLO}}$ (states.Ry^{-1}f.u.$^{-1}$)	Θ_D (K)
4.10	31.4	1.50	181.5	71.3	412
4.85	23.8	1.44	137.6		418
5.10	21.0	1.60	121.4	162.5	404
5.14	15.1	1.56	87.3		407
5.43	11.2	1.77	64.7		390
5.59	25.4	2.05	146.8		371
5.76	38.5	2.21	222.5		362
6.10	59.0	2.79	341.1	343.1	335

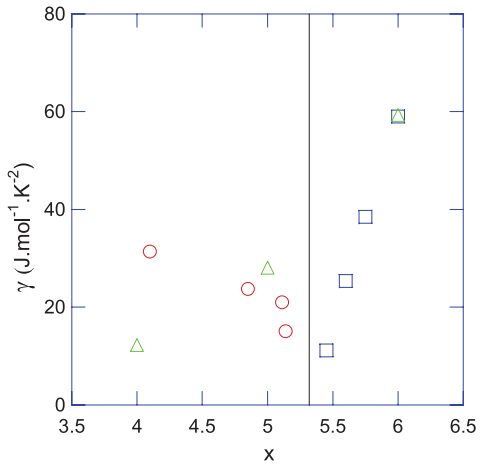

FIG. 11. (Color online) Sommerfeld coefficient γ of $Ba_8Au_xSi_{46-x}$ as a function of the Au concentration in the (○) n-type and (□) p-type regions. The black solid line marks the theoretical Au concentration ($x = 5.33$) where a crossover from n- to p-type is expected to occur according to the Zintl–Klemm concept. The symbols (△) refer to the theoretical values derived by the FPLO method.

the local environment in the unit cell, thereby further affecting the phonon spectrum.

A quantitative description of the temperature dependence of C_p in clathrate compounds is usually based on the Debye theory, including additional Einstein terms to take into account the thermal motion of the Ba2 atoms entrapped in the tetrakaidecahedra. After subtracting the electronic contribution γT, the lattice specific heat $C_L(T)$ can be expressed as

$$C_L = C_D + C_{Ei} = \frac{12\pi^4 N_D k_B}{5}\int \frac{x^4 e^x dx}{(e^x-1)^2} + \sum_i p_i N_{Ei} R \left(\frac{\theta_{Ei}}{T}\right)^2 \frac{e^{\theta_{Ei}/T}}{(e^{\theta_{Ei}/T}-1)^2} \quad (3)$$

where C_D is the lattice contribution associated to the Au-Si framework described within the Debye model and C_{Ei} the Einstein contribution of the ith vibrational mode of the Ba2 atoms. Since single-crystal refinements have shown that the Ba1 atoms exhibit similar Atomic Displacement Parameter (ADP) values as those obtained for the Si atoms,[23] the Ba1 atoms can also be treated as Debye oscillators. In Eq. (3), $x = \hbar\omega/k_BT$ with $\hbar = h/2\pi$, N_D is the number of Debye oscillators per formula unit and p_i, N_{Ei}, and θ_{Ei} are the degrees of freedom, the number of Einstein oscillators, and the Einstein temperature related to the ith vibrational mode, respectively. The Einstein contribution can be visualized by plotting C_p/T^3 versus T and appears in the present case as a peak centered near 15 K [Fig. 12(b)]. Several studies carried out on Ge-based type-I clathrates have shown that the thermal motion of Ba2 atoms can be satisfactorily modeled by separating the in-plane from the out-of-plane vibrations.[9,32] In the present case, the two-dimensional in-plane and one-dimensional out-of-plane motions are thus modeled by two Einstein temperatures $\theta^{\parallel}_{E1}$ and $\theta^{\perp}_{E2}$, respectively, with the degrees of freedom and the number of Einstein oscillators fixed to $p^{\parallel}_1 N^{\parallel}_{E1} = 2 \times 6$ and $p^{\perp}_2 N^{\perp}_{E2} = 1 \times 6$. The $\theta^{\parallel}_{E1}$ and $\theta^{\perp}_{E2}$ values inferred from least-square fits to the data according to Eq. (3) for the $x = 4.10$, 4.85, 5.59, and 6.10 samples are listed in Table V. These values are in very good agreement with the phonon modes revealed by

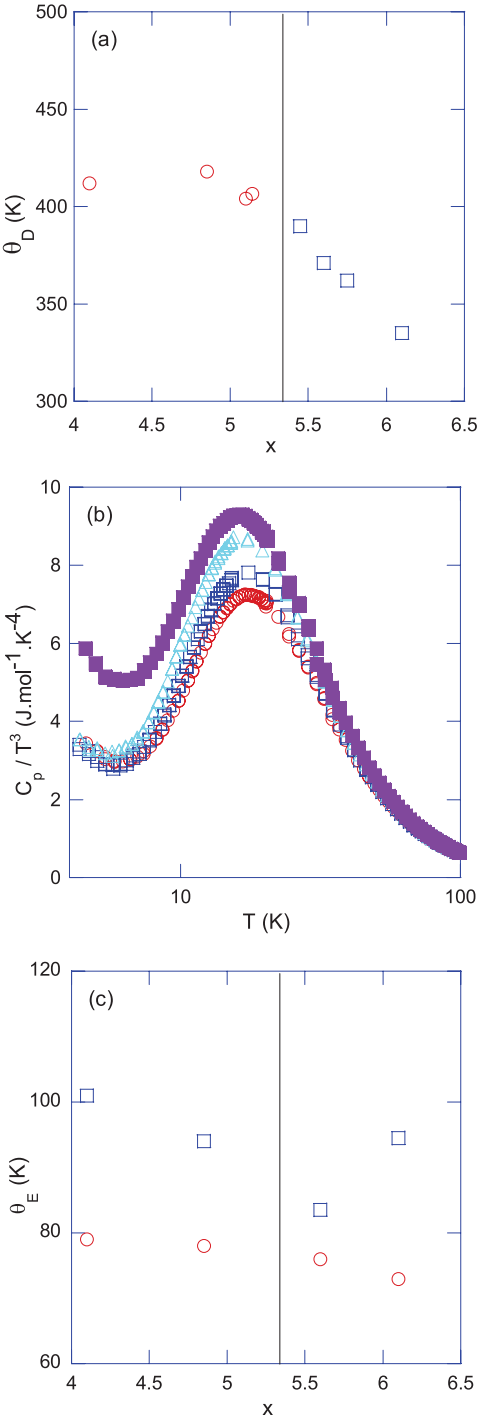

FIG. 12. (Color online) (a) Debye temperatures θ_D inferred from analyses of the low-temperature specific heat data as a function of the Au content. (b) C_p/T^3 versus T for the (○) $x = 4.10$, (□) $x = 4.85$, (△) $x = 5.59$, and (■) $x = 6.10$ samples to highlight the extra contribution to the specific heat originating from the Ba2 atoms. (c) Einstein temperatures (○) $\theta^{\parallel}_{E1}$ and (□) $\theta^{\perp}_{E2}$ derived from specific heat data using Eq. (3) as a function of the Au content. In both panels, the black line delineates the n- and p-type regions.

TABLE V. Values of the Debye temperatures θ_D and Einstein temperatures ($\theta_{E2}^{\parallel}$ and $\theta_{E2}^{\perp}$) derived from analyses of the specific heat according to Eq. (5). The corresponding phonon modes measured by Raman spectroscopy are given for comparison purposes (Ref. 13).

Au content from WDXS	θ_D (K)	$\theta_{E2}^{\parallel}$ (K)	$\theta_{E2}^{\perp}$ (K)	Raman modes (K)
4.10	358	79	101	75 and 102
4.85	353	78	94	77 and 105
5.59	343	76	84	
6.10	326	73	95	73 and 101

Raman spectroscopy experiments carried out on $x = 4.0$, 5.0, and 6.0 samples (Table V).[13] As shown in Fig. 12(c), the values of $\theta_{E1}^{\parallel}$ decrease continuously with the Au content without exhibiting any abrupt change at the n-type-p-type transition. The observed decrease may be correlated to the increase of the cage volume upon alloying with Au, as shown by single-crystal x-ray diffraction and by our PXRD data.[23] This volume change implies an increase in the in-plane thermal motion characterized by lower Einstein temperatures. It contrasts with the dependence of $\theta_{E2}^{\perp}$, which first decreases with x up to $x = 5.59$ before increasing at higher Au contents. While the decrease in the n-type region may also be associated with the larger volume of the cages, the increase in $\theta_{E2}^{\perp}$ for $x \geqslant 5.59$ may be related to the presence of Au atoms on both the 6c and the 24k sites and/or to the saturation of the lattice parameter in this composition range (see Table I and Fig. 4). In any case, our results suggest that substituting with Au affects the out-of-plane vibrations more strongly than the in-plane motion.

Figure 13(a) displays the temperature dependence of the total thermal conductivity. Below $x = 5.43$, all the samples exhibit a temperature dependence typical for the phonon conductivity in crystalline insulators, characterized by a pronounced maximum at low temperatures followed by a drastic decrease due to an increasing amount of Umklapp scattering events. The observed differences in the values of these dielectric maxima are probably related to variations in the microstructure of the samples. The values reached appear to be strongly influenced by the grain size as well as the amount of secondary phases, which differ across this series of samples. Above $x = 5.43$, however, the crystalline peak disappears, and the thermal conductivity increases in the whole temperature range. The sample with $x = 5.43$ thus appears to be at the border of these two different regimes since a maximum, though much weaker, is still discernable.

The detailed analysis of the Hall-effect and thermopower data has shown that a model assuming a single parabolic band with dominant acoustic phonon scattering describes the electrical properties of these samples quite well. This model can be extended to the thermal transport to accurately assess the lattice thermal conductivity, κ_L, by subtracting the electronic contribution, κ_e, calculated via the Wiedemann–Franz law, $\kappa_e = LT/\rho$. Within the above-mentioned assumptions, the Lorenz number, L, obtained via solutions of the Boltzmann transport equation, is expressed as[36]

$$L = \frac{k_B^2}{e^2} \frac{(1+\lambda)(3+\lambda)F_\lambda(\eta)F_{2+\lambda}(\eta) - (2+\lambda)^2 F_{1+\lambda}(\eta)^2}{(1+\lambda)^2 F_\lambda(\eta)^2}. \quad (4)$$

At low temperatures, L was assumed to be constant and equal to the value calculated at 300 K by taking $\lambda = 0$ and using the η values derived from the thermopower data using Eq.(1) (Table III). The L values significantly differ from that of a degenerate electron gas in a pure metal ($L = L_0 = 2.44 \times 10^{-8}$ V^2.K^{-2}). The metallic behavior of the $x = 4.10$ sample indicates that assuming $L = L_0$ at low temperatures is reasonable in this case.

The temperature dependences of κ_e and κ_L are shown in Figs. 13(b) and 13(c), respectively. Below $x = 5.43$, the curves are similar, indicating a minimal influence of the Au content on the lattice contribution, as expected from such close chemical compositions. However, a further increase in x results in a significant drop in κ_L, the lowest values being achieved at $x = 6.10$. The fact that the behavior of the thermal conductivity varies with the type of charge carrier has already been observed in other type-I clathrate compounds, e.g. $Ba_8Ga_{16}Ge_{30}$, $Ba_8Ni_{6-x}Ge_{40+x}$ and $Ba_8Ga_{16}Sn_{30}$ where p-type conduction is synonymous with glasslike behavior.[37–39] Though the exact reason of the difference between n- and p-type materials is not fully understood, it was suggested that hole carriers might help increase the intensity of the coupling between the guest vibrations and the framework, thereby efficiently reducing the lattice thermal conductivity.[40] Another ingredient which has been invoked to explain glasslike behavior is a strong interaction between phonons and charge carriers. This mechanism, related to changes in the effective mass m^*, has been suggested as being solely responsible for the shift from crystalline to glasslike behavior in the $Eu_8Ga_{16}Ge_{30}$ and $Ba_8Ni_{6-x}Ge_{40+x}$ systems.[37,39,41–43] As pointed out by Avila *et al.*,[40] the overall picture may be more complex, and several mechanisms may simultaneously contribute to achieve glasslike behavior, each of them dominating a different temperature range and varying with the composition of the clathrate. This complexity is further demonstrated by results obtained in n-type $Ba_8Ga_{16}Ge_{30}$, where a crossover to a glasslike regime has been observed below 2 K even though a crystalline peak is clearly present near 15 K.[40]

Each of these mechanisms nevertheless leads to signatures which can be unveiled either by crystallographic studies or via specific-heat data, which we now discuss for $Ba_8Au_xSi_{46-x}$ in light of the results mentioned above. A first essential feature is the crystalline peak still discernable in the p-type $x = 5.43$ sample, which indicates a gradual evolution from crystallike to glasslike dependence. This progressive disappearance closely resembles the one observed in the $Sr_8Ga_{16}Si_{30-x}Ge_x$ system, where a clear correlation between the free space for the Sr atoms in the cages and a continuous transition from on-center harmonic to off-center anharmonic vibrations was

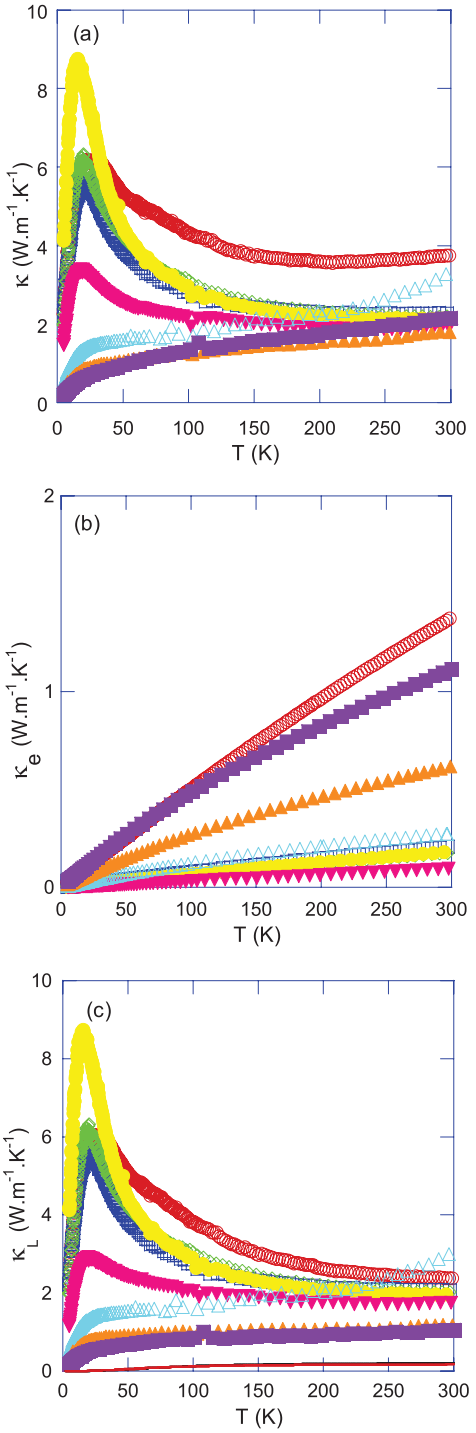

FIG. 13. (Color online) Temperature dependence of the (a) total, (b) electronic, and (c) lattice thermal conductivities of the $Ba_8Au_xSi_{46-x}$ samples for (○) $x = 4.10$, (□) $x = 4.85$, (◇) $x = 5.10$, (●) $x = 5.14$, (▼) $x = 5.43$, (△) $x = 5.59$, (▲) $x = 5.76$, and (■) $x = 6.10$. The solid red (dark gray) and black curves stand for the temperature dependence of the thermal conductivity in the amorphous limit according to Eq.(5) and calculated for the compositions $x = 4.10$ and 6.10, respectively.

uncovered.[44] It is this transition which leads to a strengthening of the coupling between the low-energy modes associated to the guest atoms and the acoustic modes of the cages. X-ray diffraction analyses indeed revealed that Sr atoms are located at the off-centered 24*k* site with $\frac{1}{4}$ occupancy. However, this feature is not restricted to $Sr_8Ga_{16}Si_{30-x}Ge_x$ and has also been observed in the *n*-type $Sr_8Ga_{16}Ge_{30}$, *n*-type $Eu_8Ga_{16}Ge_{30}$, and *p*-type $Ba_8Ga_{16}Sn_{30}$.[40,45–47] The distinct position away from the centered 6*d* site gives rise to a dynamic motion of the guest ions via tunneling among the fourfold split sites, leaving two signatures in the thermodynamic properties at low temperatures.[48–50] The first one is associated with tunneling states, yielding an extra contribution to the specific heat at low temperatures via a T-linear term $C_{TS} = DT$, which convolves with the conventional electronic contribution to the specific heat $C_e = \gamma T$.[48] It is therefore usually difficult to extract this term from the experimental data. Nevertheless, this contribution has been shown to dominate the low-temperature $C_p(T)$ data in the above-mentioned clathrates resulting in an apparent γ value anomalously larger than that expected from the free electron model.[47,48] The second signature is related to the inadequacy of Eq. (3) to describe the peak observed in the $C_p(T)/T^3$ data as demonstrated in the $Sr_8Ga_{16}Si_{30-x}Ge_x$ system.[44] In the $Ba_8Au_xSi_{46-x}$ compounds, no hints of the presence of these two signatures could be resolved, neither in the γ values, which can be explained solely by the variations in the density of states with x, specifically at large x values, nor in the $C_p(T)/T^3$ data, which can be well described by Eq. (3), regardless of the composition. In addition, our crystallographic investigations together with those of Jaussaud *et al.*[23] could not provide any indications of a split position of the Ba2 atoms, usually reflected by abnormally large thermal ellipsoids.

The absence of tunneling states in the present system thus points to different mechanisms responsible for the observed crossover. Additional phonon scattering off the Au/Si sites and naturally linked to the presence of Au atoms on both the 6*c* and 24*k* sites for $x > 5.43$ may play a significant role in the disappearance of the crystalline peak. However, it is not yet clear whether such a small number of Au atoms (∼0.3 for $x = 5.89$,[23] ∼0.5 for $x = 6.10$) is able to have such a profound effect on the lattice thermal conductivity. Additionally, an enhanced phonon-charge carrier coupling may also contribute to the lower $\kappa(T)$ values and, as in the *p*-type $Ba_8Ni_{6-x}Ge_{40+x}$ clathrates,[39] may be reflected by the larger effective mass in the *p*-type $Ba_8Au_xSi_{46-x}$ samples (see Table III). It should be kept in mind that, in the present system, it is not fully clarified whether these mechanisms lead to a temperature dependence which only mimics that of glasslike systems, as already seen, e.g. in skutterudite compounds,[51] or whether they result in a real glassy dependence, as observed in some other type-I clathrates. To settle this issue, it would be illuminating to grow single crystals of *p*-type $Ba_8Au_xSi_{46-x}$ clathrates and measure the thermal conductivity at lower temperatures to possibly uncover a T^2 dependence which represents the hallmark of glassy systems.[52]

As shown in Fig. 13(c), the very low $\kappa_L(T)$ values approach the amorphous limit of the lattice thermal conductivity $\kappa_{\min}$, calculated for the $x = 4.10$ and 6.10 samples by using the formulation developed by Cahill *et al.*,[53]

$$\kappa_{\min} = \left(\frac{\pi}{6}\right)^{\frac{1}{3}} k_B V^{-\frac{2}{3}} \sum_i v_i \left(\frac{T}{\theta_i}\right)^2 \int_0^{\theta_i/T} \frac{x^3 e^x}{(e^x - 1)^2} dx \qquad (5)$$

where the summation is performed over one longitudinal and two transverse modes. Here, V stands for the average volume per atom, and $\theta_i = v_i(\hbar/k_B)(6\pi^2/V)^{1/3}$ and v_i are the Debye temperature and the sound velocity associated to each mode. The transverse and longitudinal velocities of sound, v_T and v_L, respectively, can be related to the averaged velocity of sound v via the formalism developed by Slack *et al.*[54]

$$\frac{3}{v^3} = \frac{2}{v_T^3} + \frac{1}{v_L^3}. \tag{6}$$

In Eq. (6), we used the value of v obtained from the Debye temperature, derived by analyzing the specific heat data. Note that $\kappa_{\min}$ shows only a tiny composition dependence on going from $x = 4.10$ to 6.10. Clearly, the phonon mean free path is strongly limited in the p-type samples with respect to the n-type analogues. Thus, substitution of Si by Au appears as an efficient way to achieve lower thermal conductivity values in Si-based type-I clathrates.

IV. CONCLUSION

We have reported a detailed investigation of the evolution of the low-temperature transport properties in the type-I clathrate phase $Ba_8Au_xSi_{46-x}$ for $4.10 \leqslant x \leqslant 6.10$ to address the x dependence of the electronic properties along with the thermoelectric potential of these materials. The chemical and structural characterizations have shown that the homogeneity range in this system extends from $x = 3.63$ to $x = 6.10$ at 900 °C and that Au atoms preferentially occupy the 6*c* site, even though a small amount was also refined at the 24*k* site. The transport data could be satisfactorily described within a single-parabolic-band model, assuming that the mobility of the charge carriers is solely limited by acoustic-phonon scattering. In agreement with our first-principles calculations, an n-type-p-type transition was confirmed to set in near a critical concentration $x = 5.33$, suggesting that this system follows the Zintl–Klemm concept. The results revealed a complex influence of Au on the thermal transport, which evolves from crystallike behavior in the n-type samples to a glasslike one in the p-type samples at high x values. Of the different mechanisms which may play a role in this crossover, both a higher degree of disorder and an enhanced phonon-charge carrier coupling may be operating. The large electrical resistivity of these samples appears as the limiting factor in achieving high ZT values (the maximum ZT is ~0.10 at 300 K in the $x = 5.59$ sample). In order to improve the thermoelectric performance at higher temperatures, one interesting possibility may be the investigation of double-substituted clathrates Au-Ga. This may not only lead to higher power factor but may also provide further information as for the intriguing evolution of the lattice thermal conductivity with the Au content. In this regard, the $Ba_8Au_xSi_{46-x}$ phase offers an interesting experimental window to get a deeper understanding of the correlations between the crystal structure, the nature of the electrical conduction, and the thermal transport in type-I clathrates.

ACKNOWLEDGMENTS

The authors thank Petra Scheppan and members of the Kompetenzgruppe Struktur for providing experimental support and Y. Prots for the single-crystal x-ray diffraction measurements. C.C. acknowledges the financial support of the CNRS-MPG program. M.B. and Yu.G. acknowledge financial support by the Deutsche Forschungsgemeinschaft (SPP 1415, Kristalline Nichtgleichgewichtsphasen—Präparation, Charakterisierung und *in situ*-Untersuchung der Bildungsmechanismen).

*Corresponding author: christophe.candolfi@cpfs.mpg.de

[1] S. Yamanaka, E. Enishi, H. Fukuoka, and M. Yasukawa, Inorg. Chem. **39**, 56 (2000).
[2] S. Yamanaka, Dalton Trans. **39**, 1901 (2010), and references therein.
[3] K. Tanigaki, T. Shimizu, K. M. Itoh, J. Teraoka, Y. Moritomo, and S. Yamanaka, Nature Mat. **2**, 653 (2003).
[4] R. Lortz, R. Viennois, A. Petrovic, Y. Wang, P. Toulemonde, C. Meingast, M. M. Koza, H. Mutka, A. Bossak, and A. San Miguel, Phys. Rev. B **77**, 224507 (2008).
[5] H. Fukuoka, J. Kiyoto, and S. Yamanaka, J. Solid State Chem. **175**, 237 (2003).
[6] Y. Li, R. Zhang, Y. Liu, N. Chen, Z. P. Luo, X. Ma, G. Cao, Z. S. Feng, C. R. Hu, and J. H. Ross, Phys. Rev. B **75**, 054513 (2007).
[7] Y. Li, Y. Liu, N. Chen, G. Cao, Z. Feng, and J. H. Ross, Phys. Lett. A **345**, 398 (2005).
[8] N. Kamakura, T. Nakano, Y. Ikemoto, M. Usuda, H. Fukuoka, S. Yamanaka, S. Shin, and K. Kobayashi, Phys. Rev. B **72**, 014511 (2005).
[9] M. Christensen, S. Johnsen, and B. B. Iversen, Dalton Trans. **39**, 978 (2010).
[10] G. S. Nolas, G. A. Slack, and S. B. Schujman, in *Semiconductors and Semimetals*, edited by T. M. Tritt, Vol. 69 (Academic Press, San Diego, CA, 2001), p. 255.
[11] H. J. Goldsmid, in *Thermoelectric Refrigeration* (Temple Press Books Ltd., London, 1964), p. 43.
[12] C. Candolfi, U. Aydemir, A. Ormeci, M. Baitinger, N. Oeschler, F. Steglich, and Yu. Grin, Phys. Rev. B **83**, 205102 (2011).
[13] J. S. Tse, T. Iitaka, T. Kume, H. Shimizu, K. Parlinski, H. Fukuoka, and S. Yamanaka, Phys. Rev. B **72**, 155441 (2005).
[14] N. Tsujii, J. H. Roudebush, A. Zevalkink, C. A. Cox-Uvarov, G. J. Snyder, and S. M. Kauzlarich, J. Solid State Chem. **184**, 1293 (2011).
[15] I. Zeiringer, E. Bauer, A. Grytsiv, P. Rogl, and H. Effenberger, Jpn. J. Appl. Phys. **50**, 05FA01 (2011).
[16] J. H. Roudebush, E. S. Toberer, H. Hope, G. J. Snyder, and S. M. Kauzlarich, J. Solid State Chem. **184**, 1176 (2011).
[17] D. Shu-Kang, T. Xin-Feng, and T. Run-Sheng, Chin. Phys. B **18**, 3084 (2009).
[18] V. L. Kuznetsov, L. A. Kuznetsova, A. E. Kaliazin, and D. M. Rowe, J. Appl. Phys. **87**, 7871 (2000).
[19] N. P. Blake, D. Bryan, S. Latturner, L. Møllnitz, G. D. Stucky, and H. Metiu, J. Chem. Phys. **114**, 10063 (2001).

[20]E. S. Toberer, M. Christensen, B. B. Iversen, and G. J. Snyder, Phys. Rev. B **77**, 075203 (2008).
[21]J. Martin, H. Wang, and G. S. Nolas, Appl. Phys. Lett. **92**, 222110 (2008).
[22]H. Zhang, H. Borrmann, N. Oeschler, W. Schnelle, C. Candolfi, M. Schmidt, U. Burkhardt, M. Baitinger, and J. T. Zhao, Yu. Grin, Inorg. Chem. **50**, 1250 (2011).
[23]N. Jaussaud, P. Gravereau, S. Pechev, B. Chevalier, M. Ménétrier, P. Dordor, R. Decourt, G. Goglio, C. Cros, and M. Pouchard, C. R. Chimie **8**, 39 (2005).
[24]L. G. Akselrud, P. Y. Zavalii, Yu. Grin, V. K. Pecharsky, B. Baumgartner, and E. Wölfel, Mater. Sci. Forum **133–136**, 335 (1993).
[25]K. Koepernik and H. Eschrig, Phys. Rev. B **59**, 1743 (1999).
[26]J. P. Perdew and Y. Wang, Phys. Rev. B **45**, 13244 (1992).
[27]K. A. Kovnir and A. V. Shevelkov, Russ. Chem. Rev. **73**, 923 (2004).
[28]W. Jung, J. Lörincz, R. Ramlau, H. Borrmann, Yu. Prots, F. Haarmann, W. Schnelle, U. Burkhardt, M. Baitinger, and Yu. Grin, Angew. Chem. **119**, 6846 (2007).
[29]G. Cordier and P. Woll, J. Less-Comm. Met. **169**, 291 (1991).
[30]N. Melnychenko-Koblyuk, A. Grytsiv, P. Rogl, E. Bauer, R. Lackner, E. Royanian, M. Rotter, and G. Giester, J. Phys. Soc. Jpn. **77**, 54 (2008).
[31]Y. Liang, B. Böhme, M. Reibold, W. Schnelle, U. Schwarz, M. Baitinger, H. Lichte, and Yu. Grin, Inorg. Chem. **50**, 4523 (2011).
[32]U. Aydemir, C. Candolfi, H. Borrmann, M. Baitinger, A. Ormeci, W. Carrillo-Cabrera, C. Chubilleau, B. Lenoir, A. Dauscher, N. Oeschler, F. Steglich, and Yu. Grin, Dalton Trans. **39**, 1078 (2010).
[33]C. Candolfi, U. Aydemir, M. Baitinger, N. Oeschler, F. Steglich, and Yu. Grin, J. Elec. Mater. **39**, 2039 (2010).
[34]A. Kerkau, D. Grüner, A. Ormeci, Y. Prots, H. Borrmann, W. Schnelle, E. Bischoff, Y. Grin, and G. Kreiner, Z. Anorg. Allg. Chem. **635**, 637 (2009).
[35]M. Falmbigl, G. Rogl, P. Rogl, M. Kriegisch, H. Müller, E. Bauer, M. Reinecker, and W. Schranz, J. Appl. Phys. **108**, 043529 (2010).
[36]V. I. Fistul, *Heavily Doped Semiconductors* (Plenum Press, New York, 1969), p. 139.
[37]A. Bentien, M. Christensen, J. D. Bryan, A. Sanchez, S. Paschen, F. Steglich, G. D. Stucky, and B. B. Iversen, Phys. Rev. B **69**, 045107 (2004).
[38]M. Christensen, N. Lock, J. Overgaard, and B. B. Iversen, J. Am. Chem. Soc. **128**, 15657 (2006).
[39]A. Bentien, S. Johnsen, and B. B. Iversen, Phys. Rev. B **73**, 094301 (2006).
[40]M. A. Avila, K. Suekuni, K. Umeo, H. Fukuoka, S. Yamanaka, and T. Takabatake, Phys. Rev. B **74**, 125109 (2006).
[41]V. Pacheco, A. Bentien, W. Carrillo-Cabrera, S. Paschen, F. Steglich, and Yu. Grin, Phys. Rev. B **71**, 165205 (2005).
[42]A. Bentien, V. Pacheco, S. Paschen, Yu. Grin, and F. Steglich, Phys. Rev. B **71**, 165206 (2005).
[43]S. Paschen, W. Carrillo-Cabrera, A. Bentien, V. H. Tran, M. Baenitz, Yu. Grin, and F. Steglich, Phys. Rev. B **64**, 214404 (2001).
[44]K. Suekuni, M. A. Avila, K. Umeo, and T. Takabatake, Phys. Rev. B **75**, 195210 (2007).
[45]B. C. Sales, B. C. Chakoumakos, R. Jin, J. R. Thompson, and D. Mandrus, Phys. Rev. B **63**, 245113 (2001).
[46]K. Suekuni, M. A. Avila, K. Umeo, H. Fukuoka, S. Yamanaka, T. Nakagawa, and T. Takabatake, Phys. Rev. B **77** 235119 (2008).
[47]M. A. Avila, K. Suekuni, K. Umeo, H. Fukuoka, S. Yamanaka, and T. Takabatake, Appl. Phys. Lett. **92**, 041901 (2008).
[48]J. Xu, J. Tang, K. Sato, Y. Tanabe, H. Miyasaka, M. Yamashita, S. Heguri, and K. Tanigaki, Phys. Rev. B **82**, 085206 (2010).
[49]K. Umeo, M. A. Avila, T. Sakata, K. Suekuni, and T. Takabatake, J. Phys. Soc. Jpn. **74**, 2145 (2005).
[50]U. Buchenau, Yu. M. Galperin, V. L. Gurevich, and H. R. Schober, Phys. Rev. B **43**, 5039 (1991).
[51]C. Uher, Semiconductors and Semimetals **69**, 139 (2001).
[52]J. L. Cohn, G. S. Nolas, V. Fessatidis, T. H. Metcalf, and G. A. Slack, Phys. Rev. Lett. **82**, 779 (1999).
[53]D. G. Cahill, S. K. Watson, and R. O. Pohl, Phys. Rev. B **46**, 6131 (1992).
[54]G. A. Slack and V. G. Tsoukala, J. Appl. Phys. **76**, 1665 (1994).